Self-similar bending in a flow: The axisymmetric case

Silas Alben[a)]
School of Mathematics, Georgia Institute of Technology, Atlanta, Georgia 30332-0160, USA

(Received 23 March 2010; accepted 24 June 2010; published online 12 August 2010)

We study how sheets roll up into conical configurations when exposed to fluid flows using simulations and analysis. The simulations couple the bending of thin sheets to axisymmetric flows with vortex shedding. We find quasisteady flows with vortex ring wakes in which the radii of the rings scale with the radii of the cone bases. The cone angles scale with the dimensionless flow speed raised to the power $-1/3$. The drag coefficients for the cones scale with flow speed to the power -1. We find good agreement with the previously published experimental results. The scalings we have found result from a self-similar behavior of the flow at the outer edges of the cones, with length scales set by the radii of the vortex rings in the wakes. © *2010 American Institute of Physics*.
[doi:10.1063/1.3467494]

I. INTRODUCTION

Recent studies have suggested that many leaf structures are adapted to the fluid forces they experience.[1] With their large surfaces, leaves are well suited to collect sunlight and perform gaseous exchange with the atmosphere. They perform these functions while exposed to flows of air and water, which are sometimes fast and rapidly fluctuating, leading to large forces on leaf supporting structures (stems, branches, trunks, holdfasts, etc.).[2] Flexibility allows leaves to become streamlined in fluid flows by bending, which greatly reduces the fluid forces experienced by leaves' supporting structures.[3,4]

Vogel[3] described a tendency for certain tree leaves to roll up into conical shapes in high winds. The cones tightened with increasing wind speed, as increasing fluid pressure forces overcame the leaves' resistances to bending. Vogel[2] also collected data on fluid drag versus flow speed from a variety of studies on leaves and sessile organisms. In most cases, drag grew more slowly with flow speed than the quadratic scaling typical of rigid objects at high Reynolds number (Re). Alben, Shelley, and Zhang studied a two-dimensional version of the problem experimentally and theoretically.[4,5] The experiments measured the shapes and drag for thin, flexible glass fibers in a soap film flow tunnel and found a substantial reduction in drag growth from the quadratic rigid-body scaling. Free streamline models showed that drag grows as the 4/3 power of flow speed (so the drag coefficient decreases as the $-2/3$ power of flow speed), and simultaneously the shapes are self-similar, collapsing when their distances relative to the center hold point are scaled by flow speed to the $-2/3$ power. Zhu's two-dimensional immersed boundary simulations explored the dependence of the drag scaling on Reynolds number and found power law exponents for drag that decreased monotonically from 2 down to 1.56 as Re increased from 10 to 800.[6]

In Ref. 7, Schouveiler and Boudaoud studied the rolling up of plastic sheets experimentally and theoretically. They mounted circular sheets at their centers in a water tunnel. The sheets were cut along a radius, and in a steady flow, they rolled up into conical configurations. Similar to Vogel's leaves,[3] the opening angle decreased with increasing flow speed. They formulated two models with potential flows coupled to the bending of a conical elastic sheet. In the first, they modeled the flow as a potential flow in an infinite conical domain, so the streamlines passing along the cone surface remain straight out to infinity. The arbitrary prefactor of this potential flow is determined by matching a fixed flow speed at the outer edge of the cone. The second model uses a momentum conservation argument with a single fitting parameter.[8] Considering the simplicity of the flow models, they obtained a very reasonable agreement between their models and the experimental data in terms of the scaling of the cone angle and the drag on the cone. A more recent work (published during the revision of the present paper) includes experiments on a different (quasi)axisymmetric geometry, in which a circular disk is cut in many places along its radius and thus bends along each radius as a tapered beam.[9] This extensive study also includes a new dimensional analysis of two-dimensional (2D) and axisymmetric experimental results that takes into account three-dimensional and blockage effects, and a theoretical analysis of the disk with many sections using a momentum conservation argument.

In this work, we study the axisymmetric bending problem similarly to Ref. 7. In particular, we use the same model for the elastic bending of the cone. However, we replace their approximate potential flow model with a more detailed flow model. Our model solves a version of the unsteady incompressible Euler equations, which includes vortex shedding, with appropriate boundary conditions. We perform axisymmetric simulations of inviscid flows past conical sheets that shed vortex sheets at their edges, according to the Kutta condition. This flow model was developed previously by Nitsche and Krasny to simulate the axisymmetric flow past a rigid body (a piston tube), and the results agreed very well with experiments in terms of the detailed shapes of the vortex sheets as they rolled up into vortex rings.[10]

In Sec. II we present the coupled flow-body model and

[a)]Electronic mail: alben@math.gatech.edu.

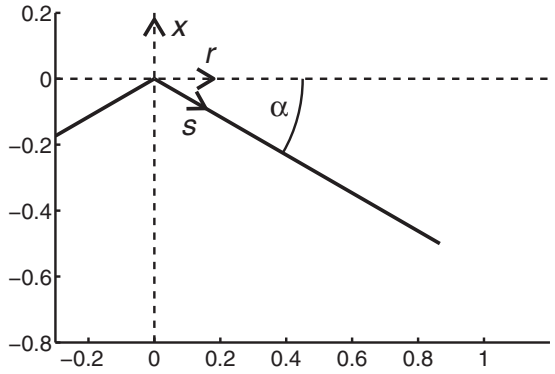

FIG. 1. Coordinate system used in this work for the conical geometry. The angle α gives the deviation of the cone (solid line) from the flat state. The axial and radial coordinates are x and r, and s is the distance from the cone apex in the x-r plane.

numerical method. Section III gives the main results: the scaling of cone angle, drag, and pressure distribution with the dimensionless flow speed. For ease of comparison with Ref. 7, we use the dimensionless flow speed squared, $\mathcal{N}$. In Sec. IV we search for similarity solutions to the steady equations, where the length scale of similarity is that of the trailing vortex ring wake. We find that we are able to predict the scaling of cone angle and drag from the similarity solution. We compare our results with the results in Ref. 7 and the two-dimensional results in Refs. 4 and 5.

II. AXISYMMETRIC FLOW MODEL

We now give the coupled flow-body model that describes the axisymmetric bending of a sheet in a quasisteady flow. Our model for the force balance between the bending and the fluid pressure is essentially the same as that given in Ref. 7. We summarize it here for completeness.

We consider a circular sheet of radius R cut along one radial direction, which assumes a self-overlapping configuration within a one-parameter family of conical shapes. The cone deviates from the plane $x=0$ by an angle α (see Fig. 1). For the downward bending shown in Fig. 1, $\alpha<0$. Experiments on leaves[3] and plastic sheets[7] have shown that a quasiconical configuration is typical for a thin lamina held in a high speed flow. The flow is also assumed to be axisymmetric with zero swirl, which considerably simplifies the flow while retaining the essential features. While the real flow becomes unstable to nonaxisymmetric or swirling modes at large Reynolds number, we may expect that the axisymmetric, zero swirl component of the flow contains most of the decrease of fluid momentum relevant to the shape of the sheet and its drag.

Following Ref. 7, the curvature at position s along a conical surface that makes an angle α with the r axis is

$$c = \tan \alpha / s. \tag{1}$$

We express the potential energy of the system as a sum of the elastic bending energy of the cone and the work done in bending the cone from its flat state by the fluid pressure difference across it, $[p]$,

$$\mathcal{E} = \frac{1}{2} D \int_S c^2 dS - \int_0^\alpha d\alpha' \int_{S_{\alpha'}} [p] s dS_{\alpha'}. \tag{2}$$

Here, D is the bending modulus of the sheet, $S=\pi R^2$ is the total area of the conical sheet, and $S_{\alpha'}=\pi R^2 \cos \alpha'$ is the portion of the sheet's area that is exposed to the flow. As in Ref. 7, we assume that the conical sheet has a nonzero inner radius R_c. This cutoff radius is necessary to prevent the divergence of the elastic energy in Eq. (2), which scales as $\log R_c$. We nondimensionalize s as $\tilde{s}=s/R$ and $[p]$ as $[\tilde{p}]=[p]/\rho U^2$, fluid density times the square of the flow speed at infinity upstream, which is U. Time is nondimensionalized as $\tilde{t}=tU/R$.

Evaluating the elastic energy in Eq. (2) and nondimensionalizing, we have

$$\mathcal{E} = \pi D \log\left(\frac{R}{R_c}\right) \tan^2 \alpha - \rho U^2 R^3 \int_0^\alpha d\alpha' \int_{\tilde{s}=0}^{\tilde{s}=1} [\tilde{p}] 2\pi \tilde{s}^2 \cos \alpha' d\tilde{s}. \tag{3}$$

The kinetic energy of the sheet is given in terms of α by

$$\mathcal{T} = \int_0^R \frac{1}{2} \rho_s 2\pi s h \left(s \frac{d\alpha}{dt}\right)^2 ds = \frac{\pi \rho_s R^4 h}{4} \left(\frac{d\alpha}{dt}\right)^2 = \frac{\pi \rho_s R^2 U^2 h}{4} \left(\frac{d\alpha}{d\tilde{t}}\right)^2, \tag{4}$$

where h is the sheet thickness and ρ_s is the sheet density. Taking the variations of the kinetic and potential energies with respect to α yields the equation of motion of the cone according to the extended Hamilton's principle of classical mechanics. The Euler–Lagrange equation for the dynamics of α is then

$$\mathcal{M} \frac{d^2\alpha}{d\tilde{t}^2} = \frac{\sin \alpha}{\cos^3 \alpha} - 2\mathcal{N} \int_0^1 [\tilde{p}](\tilde{s},\tilde{t}) \tilde{s}^2 \cos \alpha d\tilde{s}, \tag{5}$$

where the dimensionless parameters are

$$\mathcal{M} = \frac{\rho_s R^2 U^2 h}{2D \log(R/R_c)}, \quad \mathcal{N} = \frac{\rho U^2 R^3}{D \log(R/R_c)}. \tag{6}$$

From now on, we continue to use dimensionless variables but drop tildes, for clarity. The pressure jump across the cone is obtained by solving for the inviscid flow with axisymmetric vortex sheets, similarly to Ref. 10. The flow is irrotational except for a bound vortex sheet along the cone surface and a free vortex sheet that separates from the cone's outer edge. The strength of the bound vortex sheet is determined by imposing the condition that flow does not penetrate the cone surface. The strength of the free vortex sheet is determined by imposing the Kutta condition that the flow velocity remains finite at the cone's outer edge. This sets the cumulative spatial integral of the circulation in the free vortex sheet, which is conserved at circular vortex filaments in the free sheet that move with the flow, according to Kelvin's theorem.[11] The free vortex sheet evolves according to a regularized version of the axisymmetric Biot–Savart law.

Following Ref. 10, the stream function at (x,r) due to a regularized circular vortex filament of unit strength at (x_1,r_1) is

$$\psi_\delta(x,r;x_1,r_1)=\frac{1}{4\pi}\int_0^{2\pi}\frac{rr_1\cos\theta}{\rho^2+\delta^2}d\theta, \tag{7}$$

where $\rho^2=(x-x_1)^2+r^2+r_1^2-2rr_1\cos\theta$ and δ is the vortex sheet smoothing parameter. The velocity corresponding to Eq. (7) is given by

$$u_\delta(x,r;x_1,r_1)=\frac{1}{r}\frac{\partial\psi_\delta}{\partial r}(x,r;x_1,r_1),$$

$$v_\delta(x,r;x_1,r_1)=-\frac{1}{r}\frac{\partial\psi_\delta}{\partial x}(x,r;x_1,r_1), \tag{8}$$

where u_δ is the axial component and v_δ is the radial component. Detailed formulae for (u_δ,v_δ) are given in Ref. 10. The velocity induced by the free vortex sheet is obtained by integrating over the sheet, parametrized by circulation

$$\begin{pmatrix}u^f\\v^f\end{pmatrix}(x,r)=\int_0^{\Gamma_T(t)}\begin{pmatrix}u_\delta\\v_\delta\end{pmatrix}[x,r;x_1(\Gamma,t),r_1(\Gamma,t)]d\Gamma. \tag{9}$$

Here, $\Gamma_T(t)$ is the total circulation in the free vortex sheet at time t. The velocity induced by the bound vortex sheet with strength density γ along the cone is

$$\begin{pmatrix}u^b\\v^b\end{pmatrix}(x,r)=\int_0^1\begin{pmatrix}u_0\\v_0\end{pmatrix}(x,r;s\sin\alpha,s\cos\alpha)\gamma(s,t)ds. \tag{10}$$

Here, δ is taken to be zero on the bound sheet to avoid ill-posedness in the solution of the no-penetration equation, as described in Refs. 10 and 12.

Points on the free vortex sheet are advected at the local velocities induced by the bound and free vortex sheets,

$$\frac{dx_f}{dt}=u^b(x_f,r_f)+u^f(x_f,r_f),\quad \frac{dr_f}{dt}=v^b(x_f,r_f)+v^f(x_f,r_f). \tag{11}$$

The bound vortex sheet strength is the solution to an integral equation, the no-penetration condition, which equates the components of the flow velocity and cone velocity that are normal to the cone,

$$\begin{aligned}&\int_0^1(u_0\cos\alpha-v_0\sin\alpha)\\&\quad\times(s\sin\alpha,s\cos\alpha;s'\sin\alpha,s'\cos\alpha)\gamma(s',t)ds'\\&\quad=(-u^f\cos\alpha+v^f\sin\alpha)+\cos\alpha+s\frac{d\alpha}{dt}.\end{aligned} \tag{12}$$

We have used the facts that the normal to the cone is $(\cos\alpha,-\sin\alpha)$, the component of the far-field flow speed that is normal to the cone is $-\cos\alpha$, and the speed of the cone normal to itself is $s\,d\alpha/dt$. The P in the integral in Eq. (12) denotes a principal value integral.

The strength of the free vortex sheet is represented in terms of circulation, which is conserved at each material point of the free sheet, and thus acts as a Lagrangian marker. Material points on the free vortex sheet are labeled by the total circulation in the free sheet when they are shed, which is the parametrization in Eq. (9) used to evaluate (u_f,v_f).

At each time t, the unknown parameter $\Gamma_T(t)$ is determined by the Kutta condition, which requires that the flow velocity (and γ) be finite at the cone edge. The type of singularity that occurs in γ in the absence of the Kutta condition can be inferred from the form of the kernel in the integral equation (12) for γ. The kernel can be written as a Cauchy kernel, $\sim(s-s')^{-1}$, plus a remainder with an integrable (logarithmic) singularity.[11] The Cauchy kernel leads to a generic inverse square root singularity in γ at the cone edge, which is also the singularity that occurs in the two-dimensional version of the problem.[11] As in the two-dimensional case,[12,13] we may express $\gamma(s,t)$ as $v(s,t)/\sqrt{1-s^2}$, where $v(s,t)$ is a bounded function. We solve for $v(s,t)$ using Eq. (12), together with the Kutta condition,

$$v(1,t)=0, \tag{13}$$

which removes the flow singularity at the cone edge. Equation (13) determines the value of $\Gamma_T(t)$, which appears in Eq. (12) through Eq. (9), and hence affects the value $v(1,t)$. The treatment of the Kutta condition here is thus very similar to its treatment in the two-dimensional case.[12,13]

The pressure jump across the cone surface is expressed as in Refs. 12 and 13 in terms of $\gamma(s,t)$ and the average of the slip velocities on the two sides of the cone. We denote the average of the tangential components of the flow velocities on the two sides of the cone surface as $\mu(s,t)$,

$$\begin{aligned}\mu(s,t)=&\int_0^1(u_0\sin\alpha+v_0\cos\alpha)\\&\times(s\sin\alpha,s\cos\alpha;s'\sin\alpha,s'\cos\alpha)\gamma(s',t)ds'\\&+(u^f\sin\alpha+v^f\cos\alpha)-\sin\alpha.\end{aligned} \tag{14}$$

Here, the component of the oncoming flow velocity that is tangent to the cone is $-\sin\alpha$. We denote the component of the cone velocity tangent to itself as $\tau(s,t)$. The pressure jump is then found by taking the difference in the Euler equations on the two sides of the cone surface,

$$\begin{aligned}[p](s,t)=&-\partial_t\int_1^s\gamma(s',t)ds'-\gamma(s,t)[\mu(s,t)-\tau(s,t)]\\&+\gamma(1,t)[\mu(1,t)-\tau(1,t)].\end{aligned} \tag{15}$$

In the present problem, $\tau(s,t)=0$ since the component of the cone's motion in the x-r plane is a rotation about the cone apex and is thus directed normally to the cone surface.

To summarize, Eq. (5) relates the angle of the cone to the pressure force on it. Equations (11)–(13) and (15) determine the evolution of the free vortex sheets and the pressure force on the cone, given the angle of the cone. We reduce these equations to a coupled system for the primary variables $[\alpha(t),\Gamma_T(t),v(s,t)]$, which we solve numerically on a temporal and a spatial grid.

We now discuss the temporal and spatial discretizations of the equations. The temporal discretization is as described in Ref. 12 for two-dimensional flow, so we only summarize it

here. At the beginning of each time step t_i, a new circular vortex filament is created at the cone edge. Equations (5), (12), (13), and (15) are solved simultaneously, implicitly, to determine the cone angle $\alpha(t_i)$, the vortex sheet strength $\gamma(s,t_i)$, and the total circulation $\Gamma_T(t_i)$ in the free sheet. Then the free sheet is moved to its position at time t_{i+1} using the second-order Adams–Bashforth discretization of Eq. (11). The trapezoidal rule is used to evaluate the integrals over the free vortex sheets in Eq. (11).

The implicit solution of Eq. (12) for γ uses staggered grids along the cone surface. Bound circular vortex filaments are located on a mesh, which becomes more dense near the outer edge of the cone,

$$s_j' = \cos[\pi(m-j)/2m], \quad j = 1, \ldots, m. \tag{16}$$

Equation (12) is imposed at m points between the vortex filaments,

$$s_k = \cos[\pi(m-k+1/2)/2m], \quad k = 1, \ldots, m, \tag{17}$$

similarly to Ref. 10. These m equations solve for the m unknowns, $v(s_j',t_i) = \gamma(s_j',t_i)\sqrt{1-s_j'^2}$.

The smoothing parameter δ is set to 0.1, which is sufficiently small to resolve the instantaneous forces and the locations of the vortex sheet spirals in the wake. Very good agreement was obtained between simulations and experiments in Ref. 10 for a piston flow with a higher level of regularization, $\delta=0.2$. In general, smaller δ allows one to resolve more inner turns of vortex sheet spirals, while the positions of the outer turns are only slightly changed.[14]

We start the flow from rest and increase the oncoming flow velocity smoothly to 1 as an exponential function with time constant 0.5: $U(t)=1-e^{-(t/0.5)^2}$. Assuming the cone surface is thin, we set the cone mass $\mathcal{M}$ to 0.01, a small value. For $\mathcal{M}$ in a range $\ll 1$, there is little change in the results. We set the key parameter of interest, $\mathcal{N}$, to the values $\{2^k; k=-2,-1.5,-1,\ldots,12.5,13\}$. In order to test the robustness of the results to the initial conditions, we compute three separate solutions for each value of $\mathcal{N}$ using three initial angles for the cone: $\alpha(0)=0,-0.5,-0.9$ rad.

In the simulations presented below, we take $m=55$ and $\Delta t=0.01$. Varying these parameters to increase spatial and temporal resolution, we find no significant changes in the results. Points are added to and removed from the free vortex sheet adaptively when the spacing between neighboring points is greater than $\delta/2$ or is smaller than $\delta/6$. Insertion is done with local cubic interpolation as in Refs. 10 and 13. We run each simulation until the free sheet contains 10^5 points, at which point computing the integral in Eq. (9) with direct summation $[O(N^2)]$ is very time-consuming. The number of points in the free vortex sheet grows rapidly (perhaps exponentially) with time, so even a doubling of computing power does not extend the temporal range of our results significantly.

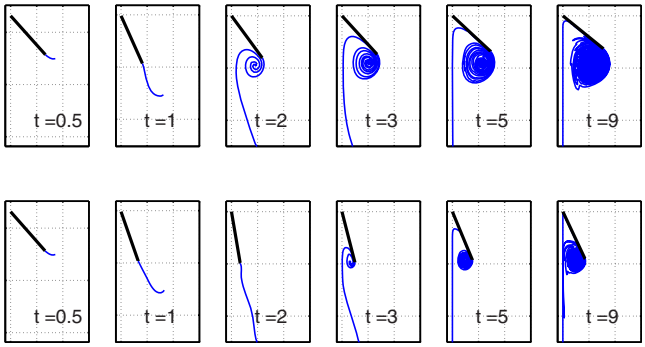

FIG. 2. (Color online) Snapshots of the vortex sheet wake [gray line (blue online)] and cone (black line) at different times for $\mathcal{N}=16$ (top row) and $\mathcal{N}=1024$ (bottom row).

III. RESULTS

In Fig. 2 we present snapshots of flows for two values of $\mathcal{N}$ at different times. The top row shows a flow for $\mathcal{N}=16$ (a moderately stiff cone) and the bottom row shows a flow for $\mathcal{N}=1024$ (a more flexible cone). In both cases, $\alpha(0)=-0.5$ rad. From the first to the second snapshot of the top row, the cone has tightened significantly. In the third through sixth snapshots, the cone reopens (or recoils) quickly at first, then rather slowly at later times. The free vortex sheet consists primarily of a single vortex ring with radius comparable to the radius of the cone base. Between $t=5$ and $t=9$, the vortex ring has grown significantly toward the axis of symmetry, but the cone angle has changed little. In the bottom row, the sequence of states is similar, but with a few important differences. The time of maximum deflection occurs later, and the angular deflection at late times is greater (as expected, since the cone is more flexible). The vortex spiral in the wake again has a radius comparable to the radius of the cone base and reaches the axis of symmetry at an earlier time.

In Fig. 3 we show the flow at a fixed time ($t=9$) for various $\mathcal{N}$. We see that the cone angle decreases with increasing $\mathcal{N}$, with a smaller rate of decrease with $\mathcal{N}$ at larger $\mathcal{N}$. In all cases, the individual turns of the vortex sheets have undergone significant infolding by $t=9$, with a somewhat jagged inner boundary, which is most apparent at the smaller values of $\mathcal{N}$ in Fig. 3. However, the overall shape of the

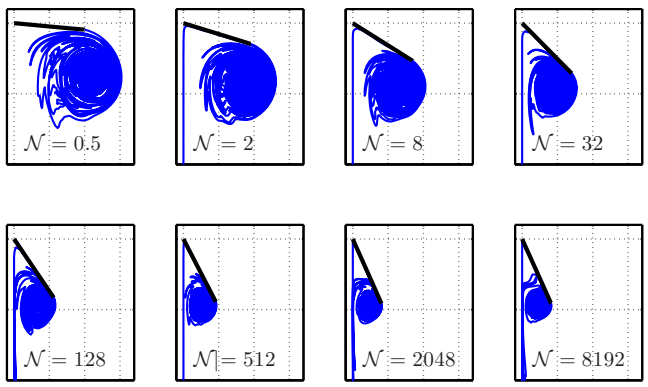

FIG. 3. (Color online) Snapshots of the vortex sheet wake [gray line (blue online)] and cone (black line) at $t=9$ for different $\mathcal{N}$.

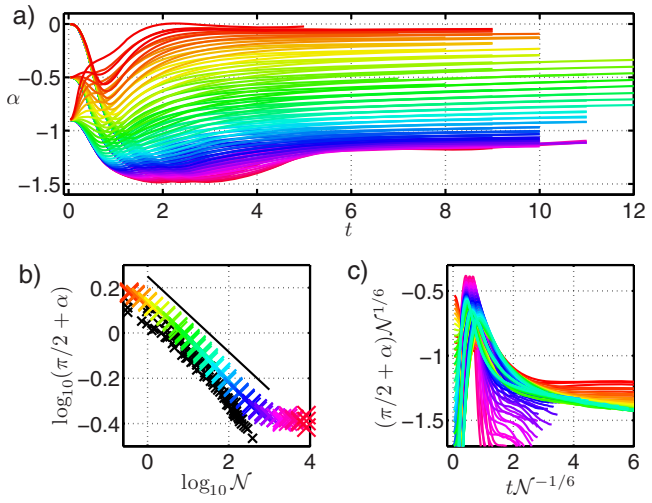

FIG. 4. (Color online) The dependence of cone angle α on time and elastohydrodynamic number $\mathcal{N}$. (a) α vs time for 31 values of $\mathcal{N}$:$\{2^k;k=-2,-1.5,-1,\ldots,12.5,13\}$ and three values of $\alpha(0)$: $\{0,-0.5,-0.9\}$. Data for each value of $\mathcal{N}$ are shown in a different shade/color; the correspondence between $\mathcal{N}$ and shade/color is given by comparing the symbols in panel (b) with the horizontal axis. (b) Quasisteady cone angle, plotted as $\log_{10}(\alpha+\pi/2)$, vs $\mathcal{N}$. The black crosses show the data from the experiment of Ref. 7. The solid line shows $\alpha+\pi/2\sim\mathcal{N}^{-1/6}$. (c) The angle data in panel (a) plotted as $(\alpha+\pi/2)\mathcal{N}^{1/6}$, with time scaled by $\mathcal{N}^{-1/6}$. The curves collapse for a wide range of intermediate values of $\mathcal{N}$.

vortex spiral is roughly circular at all $\mathcal{N}$, with a moderate elongation at the upper boundary of the spiral at larger $\mathcal{N}$.

We now quantify various quantities of interest as functions of $\mathcal{N}$. In Fig. 4(a) we show the angles of the cones versus time for 31 values of $\mathcal{N}$:$\{2^k;k=-2,-1.5,-1,\ldots,12.5,13\}$ and starting from three values of α at $t=0$: $\{0,-0.5,-0.9\}$. Data for each value of $\mathcal{N}$ are shown in a different shade/color, and the correspondence between $\mathcal{N}$ and shade/color is given by comparing the symbols in Fig. 4(b) with the horizontal axis. The curves in Fig. 4(a) show an initial period of significant fluctuations with time. For example, starting from an initial angle $\alpha=0$ at $t=0$, the curves are seen to drop to various minima ranging from -0.5 to -1.5 rad before $t=3$. The details of any one curve at early times are somewhat obscured, but we are mainly interested in certain properties of the whole set of curves, which can be seen in this superposition. Comparing the curves with different shades/colors, we can see that the shapes of the curves change smoothly with $\mathcal{N}$. In particular, we note that the higher curves, corresponding to stiffer cones (smaller $\mathcal{N}$), rise more rapidly. At later times ($t>6$), the curves approximate steady states, while, in fact, showing slow increases of α with time. Without the damping of viscosity, the inviscid vortex sheet model does not reach a steady state as readily as do laminar viscous flows. We are unable to compute steady inviscid wake flows that are consistent with the vortex sheet spiral structures shown here, so we take these slowly changing flows, at later times, as approximations to the steady flows.

Another important observation is that for $t\gtrsim 6$, there is very little dependence of the curves on the initial angle. While the three curves with a given $\mathcal{N}$ (and thus a given shade/color) start from three widely spaced values, all of the curves of a given shade/color have nearly merged into a single trajectory at later times and show little dependence on the different starting conditions. The quasisteady vortex wakes, shown in Fig. 3, have nearly the same sizes and shapes at later times, regardless of the start-up conditions. These vortex wakes serve as attracting states for the flow dynamics.

In Fig. 4(b) we plot the quasisteady cone angle from Fig. 4(a) versus $\mathcal{N}$. We define the quasisteady cone angle to be the average cone angle over the last third of the temporal data for each trajectory shown in Fig. 4(a). The three crosses of a given shade/color, corresponding to the three initial angles, generally agree quite well. At smaller $\mathcal{N}$, the curve flattens as it transitions to an undeflected cone: $\alpha=0$ [or $\log_{10}(\pi/2+\alpha)=0.196$] when $\mathcal{N}=0$ (or $\log_{10}\mathcal{N}=-\infty$). At larger $\mathcal{N}$, the curve flattens to a lower limit of α and shows a slightly increased variation with the initial conditions. The underlying reason for this lower limit of α of about $-67°$ is unclear, but may result from the fact that the circulation shed by the cone is apparently $O(1)$ even as the opening angle of the cone decreases to zero (or $\alpha\to-90°$). Even in the absence of bending rigidity, the fluid dynamics associated with the shedding of a vortex ring may resist the formation of quasisteady vortex spirals with arbitrarily small radii. Nonetheless, we obtain data over a sizable range of intermediate $\mathcal{N}$, which are well approximated by a power law behavior. The solid line gives the power law $\alpha+\pi/2\sim\mathcal{N}^{-1/6}$, which is also the power law found in the models in Ref. 7. The black crosses are the experimental data of Ref. 7, which agree well with our data over most of the range where both are given.

In this intermediate range of $\mathcal{N}$, we also notice an apparently self-similar behavior of the curves in Fig. 4(a). We rescale time by $\mathcal{N}^{-1/6}$ and the deviation of the angle from $-\pi/2$ by $\mathcal{N}^{1/6}$, and plot the results in Fig. 4(c). The curves for intermediate $\mathcal{N}$ (with shades ranging from light to dark gray, or colors ranging from yellow to blue) in Fig. 4(a) collapse reasonably well. We write a characteristic time as a ratio of a characteristic length to a characteristic speed: $T\sim L/U$. If we take U to be the dimensionless flow speed, or 1, then the fact that $T\sim\mathcal{N}^{1/6}$ implies that $L\sim\mathcal{N}^{1/6}$. If $\pi/2+\alpha\sim\mathcal{N}^{-1/6}$, then the length of the cone projected along the axis of symmetry increases approximately as $\mathcal{N}^{1/6}$, i.e., linearly with the cone deflection angle, over a range of intermediate values of $\pi/2+\alpha$. The collapse of the curves in Fig. 4(c) may indicate an intrinsic time, which is the time for the fluid stream to travel the axial length of the cone.

We now discuss the second main quantity of interest: the drag coefficient and its dependence on $\mathcal{N}$. The drag coefficient (which is the dimensionless drag, or the dimensional drag divided by ρU^2R^2, according to our previous nondimensionalization of length and pressure) is given by

$$F_x=2\pi\int_0^1[p](s,t)s\cos^2\alpha ds. \tag{18}$$

In Fig. 5 we plot the drag coefficient for the same parameters as in Fig. 4. In Fig. 5(a), during $0<t<2$, the drag coefficient has a large peak since the cone is initially far from equilibrium. Similar to the angle data, the drag coefficient data tran-

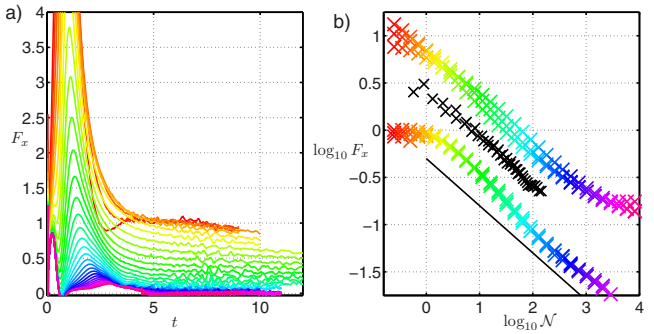

FIG. 5. (Color online) The dependence of axial drag F_x on time and elastohydrodynamic number $\mathcal{N}$. (a) F_x vs time for 31 values of $\mathcal{N}$: $\{2^k; k=-2, -1.5, -1, \ldots, 12.5, 13\}$ and $\alpha(0)=0$. Data for each value of $\mathcal{N}$ are shown in a different shade/color; the correspondence between $\mathcal{N}$ and shade/color is given by comparing the symbols in panel (b) with the horizontal axis. (b) The top three shaded/colored lines of crosses give the maximum drag in the present model. The black crosses are the experimental data of Ref. 7. The bottom set of shaded/colored crosses is the quasisteady drag in the present model. The black solid line shows $F_x \sim \mathcal{N}^{-1/2}$.

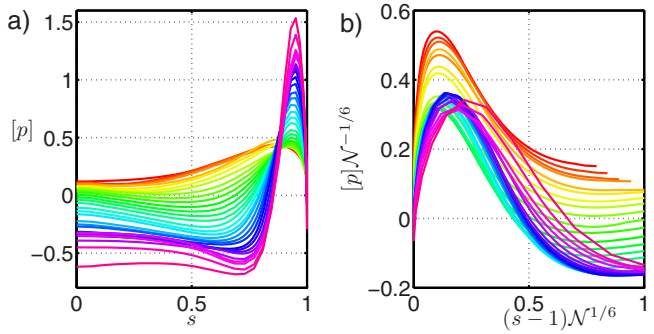

FIG. 6. (Color online) (a) The pressure loading on the cone as a function of the arc length s and the elastohydrodynamic number $\mathcal{N}$. The shades/colors correspond to $\mathcal{N}$ as in Figs. 4 and 5. (b) The data from (a) with the pressure jump scaled by $\mathcal{N}^{-1/6}$ and the arc length distance from the outer edge scaled by $\mathcal{N}^{1/6}$.

sition to a period of more gradual change for $t>5$. Small oscillations are visible in the data during this period. Since the drag force is related to the second time derivative of the cone's position, or angle, the drag coefficient varies less smoothly than the angle does with time. The oscillations are due to fluctuations inherent in the dynamics of vortex sheet spirals with many turns. Similar small oscillations were found by Krasny and Nitsche in Ref. 15 for the motion of a vortex sheet similar to our cone wakes. Their vortex sheet was not shed from a solid surface, but was instead initiated as a flat disk that quickly rolled up into a vortex ring. They found chaotic motions and jaggedness similar to that in Fig. 2 when their vortex ring had developed a number of turns comparable to that in Fig. 2.

In Fig. 5(b) the top three lines of shaded/colored crosses plot the peaks of the force curves from panel (a). The black crosses are the experimental data of Ref. 7. The bottom three lines of shaded/colored crosses plot the average drag coefficients during the last one-third of the trajectories in Fig. 5(a), which approximate the quasisteady drag coefficients. The three crosses for each value of $\mathcal{N}$ correspond to the three initial angles and show good agreement for the quasisteady drag coefficient and more variation for the peak drag coefficient, which depends more strongly on the initial conditions. For $1<\mathcal{N}<10^3$, all three sets of data are reasonably approximated by the black solid line $\sim\mathcal{N}^{-1/2}$. The models in Ref. 7 apparently gave a slightly different scaling, $\sim\mathcal{N}^{-2/3}$. Our quasisteady drag values are about half those from the experiments in Ref. 7 at corresponding $\mathcal{N}$, though the experimental data also appear to scale as $\mathcal{N}^{-1/2}$. One possible source of discrepancy is the absence of viscous dissipation in our model. Viscous dissipation can cause a multiplicative shift in the drag on objects in two-dimensional flows[4,5] by creating an additional suction in the wake. Another main source of discrepancy is that the plastic sheets in the experiment deviate from a conical shape. In the photographs of Fig. 1 of Ref. 7, the radial edges of the Mylar sheet seem to extend somewhat outward from a conical shape, which could increase the form drag of the body over that of a perfect cone. Furthermore, the layers of the cone do not overlap perfectly, so there is some airflow between the layers. Consequently, there is some deviation from axisymmetry in the flow in the experiment as well. However, it is remarkable that the photographed shapes in Ref. 7 (and Ref. 3) are as close to conical as they are. A more minor difference is in the geometry at the leading edge: in the experiment, the cone is mounted on a tube, while there is no upstream structure in the simulations. Boundary layer drag seems to be insignificant (about two orders of magnitude smaller than form drag), which was also noted in Ref. 7.

To give more insight into the drag coefficient scaling and the spatial structure of the flow, in Fig. 6 we plot the quasisteady pressure loading in Eq. (18) versus s and $\mathcal{N}$. At large $\mathcal{N}$, we find a large peak in pressure near the outer edge of the cone. The amplitude of the peak increases and its width decreases with increasing $\mathcal{N}$. In Fig. 6(b) we rescale the pressure jump by $\mathcal{N}^{-1/6}$ and the arc length distance from the outer edge by $\mathcal{N}^{1/6}$ and find a reasonable agreement of curves away from the extremes of the range in $\mathcal{N}$. We note that our pressure distributions are considerably different from those of the models in Ref. 7. Because the flow models in Ref. 7 do not include a vortex wake, their pressure distributions do not show the self-similar behavior in Fig. 6(b). For the momentum conservation model, their pressure loading is independent of the position s along the cone. For the potential flow model, their pressure loading is $[p](s)=(1-s^{2n-2})/2$, where n varies from 2 (for an undeflected cone) to 1 (for a fully deflected cone).

IV. ANALYSIS AND DISCUSSION

In Figs. 4–6 we have found that the cone angle, force, and pressure distribution are reasonably well fitted by power law behaviors with respect to $\mathcal{N}$. We now attempt to rationalize these behaviors by considering self-similar solutions to the equations when $\mathcal{N}$ is large.

We first assume that the deviation of the cone angle from the axis of symmetry, $\pi/2+\alpha$, scales as $\mathcal{N}^\beta$ for some β, which should be negative. When the cone is in equilibrium, Eqs. (5), (12), (14), and (15) become

$$\frac{\sin\alpha}{\cos^3\alpha} = 2\mathcal{N}\int_0^1 [p](s)s^2\cos\alpha ds, \tag{19}$$

$$[p](s) = -\gamma(s)\mu(s) + \gamma(1)\mu(1), \tag{20}$$

$$\int_0^1 (u_0\cos\alpha - v_0\sin\alpha) \times (s\sin\alpha, s\cos\alpha; s'\sin\alpha, s'\cos\alpha)\gamma(s')ds' = (-u^f\cos\alpha + v^f\sin\alpha) + \cos\alpha. \tag{21}$$

$$\mu(s) = \int_0^1 (u_0\sin\alpha + v_0\cos\alpha) \times (s\sin\alpha, s\cos\alpha; s'\sin\alpha, s'\cos\alpha)\gamma(s')ds' + (u^f\sin\alpha + v^f\cos\alpha) - \sin\alpha. \tag{22}$$

In addition to Eqs. (19)–(22), we have the Kutta condition (13) that sets the total circulation in the free sheet and the advection equation (11) that sets the geometry of the free sheets. Even with time eliminated and α assumed close to $-\pi/2$ (a singular limit), the system of equations is still quite complicated to solve. Although we are able to compute solutions up to $\mathcal{N}=10^4$, the minimum angle of the cone in Fig. 4 is about $-67°$, still some distance from vertical ($-90°$). Hence, our numerical solutions are still some distance from the asymptotic limit of slender cones. Nonetheless, it is useful to speculate on the reasons for the similarity behaviors in Figs. 4–6.

We first estimate the size of γ using the terms in the kinematic equation (21). The right hand side of Eq. (21) consists of the negative of the normal components of the velocities induced by the free sheet ($-u^f\cos\alpha + v^f\sin\alpha$) and the far-field flow. In the early stages of flow ($t \ll 1$), the free sheet is very short, so the velocity it induces is small. Thus, the normal component of the far-field flow, $-\cos\alpha$, dominates the right hand side. On the left hand side, the kernel in the integral scales with the radius of the cone, which has the same scaling as the right hand side, $\sim\cos\alpha$. Thus, in the early stages the bound vortex sheet strength γ is $O(1)$. This is an important difference with two-dimensional airfoil theory at low angles of attack. In the two-dimensional case, the kernel in Eq. (21) is $O(1)$, so γ is small, of the order of the angle of attack.

We now consider later times (the quasisteady state) of the axisymmetric problem, so time is $O(1)$, and the length of the free sheet is $O(1)$ [since it is advected away from the cone edge by an oncoming velocity which is $O(1)$]. The vortex sheet strength of the free sheet must be comparable to that of the bound sheet, $O(1)$, to satisfy the Kutta condition at the trailing edge. Thus, the total circulation in the free sheet is $O(1)$ even for slender cones. For $t=O(1)$, the term which is minus the component of the velocity normal to the cone induced by the free sheet ($-u^f\cos\alpha + v^f\sin\alpha$) is not negligible on the right hand side of Eq. (21). The free sheet is a vortex ring with radius $O(\pi/2+\alpha)$ (as in Fig. 3), which is at a distance $r_{\text{near}}=O(\pi/2+\alpha)$ from the trailing edge. The velocity induced by a vortex ring of circulation Γ and radius r_{near} at distances of the order of the radius from the ring is $\sim\Gamma/r_{\text{near}}$, which is $\sim 1/(\pi/2+\alpha)$ here. Farther from the trailing edge, the velocity it induces is $\sim\Gamma/1\sim 1$. To balance these flows, we expect the vortex sheet strength to be $\sim 1/(\pi/2+\alpha)$ near the trailing edge and $O(1)$ farther away. In Fig. 7(a) we plot the vortex sheet strength multiplied by $\mathcal{N}^{1/6}\sim(\pi/2+\alpha)$. The curves in shades of gray ranging from light to dark (colors ranging from yellow to blue)—corresponding to the power-law scaling regime of Figs. 4–6—overlap well near the outer edge. The light gray (yellow) curves are somewhat larger in magnitude than the dark gray (blue) curves near the outer edge, which shows that γ increases similarly to (but somewhat more slowly than) $1/(\pi/2+\alpha)$ at distances $\sim\pi/2+\alpha$ from the outer edge.

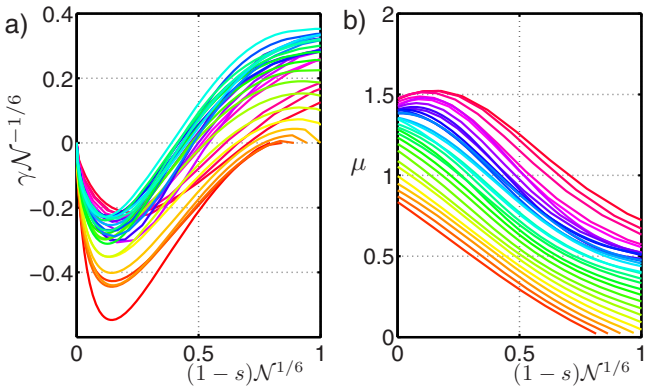

FIG. 7. (Color online) (a) The scaled vortex sheet strength on the cone $\gamma\mathcal{N}^{-1/6}$ as a function of the scaled arc length $(1-s)\mathcal{N}^{1/6}$ and the elastohydrodynamic number $\mathcal{N}$. The shades/colors correspond to $\mathcal{N}$ as in Figs. 4 and 5. (b) The averages of the flow speeds tangent to the cone, above and below the cone surface, μ, as functions of the scaled arc length $(1-s)\mathcal{N}^{1/6}$.

To obtain the pressure from Eq. (20), we now need to estimate $\mu(s)$ using Eq. (22). The right hand side of Eq. (22) contains the background flow, which is $-\sin\alpha\sim 1$, plus the tangential components of the velocities induced by the bound and free vortex sheets. Near the trailing edge vortex, the tangential velocity grows like $1/(\pi/2+\alpha)$. However, the background flow is somewhat larger in magnitude, so the overall behavior of μ is closer to $O(1)$ than to $O[1/(\pi/2+\alpha)]$. We plot μ in Fig. 7(b). Near the outer edge, the curves' magnitudes increase with $\mathcal{N}$, but the behavior is closer to $O(1)$ than to $O[1/(\pi/2+\alpha)]$.

We have seen that γ increases somewhat more slowly than $1/(\pi/2+\alpha)$, and μ behaves similarly to $O(1)$. The product of the two, which gives the pressure in Eq. (20), is well approximated by

$$[p]\sim(\pi/2+\alpha)^{-1}\sim\mathcal{N}^{-\beta}. \tag{23}$$

The pressure jump near the trailing edge is essentially a product of the vortex sheet strength near the trailing edge with the far-field flow speed (unity), which is also true in steady airfoil theory.[16]

We can now estimate the exponent β using Eq. (19), the torque balance. We have seen in Fig. 6 that the pressure loading adopts a self-similar form near the outer edge of the cone, which is where the vortex ring in the wake lies. The length scale of this region is of the same order as the radial

extent of the vortex ring, which is also the same as the radius of the base of the cone, from Fig. 3. The radius of the base of the cone scales with (half) the opening angle of the cone, or $\pi/2+\alpha \sim \mathcal{N}^{\beta}$. We make a guess that the torque provided in this region near the outer edge is comparable to the total torque on the cone. We define a new coordinate S, which is $O(1)$ in this region,

$$S = (s-1)\mathcal{N}^{-\beta}. \tag{24}$$

We also define a rescaled pressure function that is $O(1)$ as $\pi/2+\alpha \to 0$,

$$[P](S) = \mathcal{N}^{-\beta}[p][s(S)]. \tag{25}$$

We now insert $[P]$ into Eq. (19), write the integral in terms of S, and use the approximations $\cos\alpha \sim \pi/2+\alpha \sim \mathcal{N}^{\beta}$, $\sin\alpha \sim 1$. We obtain

$$\mathcal{N}^{-3\beta} \sim \mathcal{N}^{1+3\beta}\int_{-\infty}^{0}[P](S)S^2 dS. \tag{26}$$

The integral is independent of $\mathcal{N}$, so a balance requires that $\beta=-1/6$. We can use this value of β to explain the drag coefficient scaling shown in Fig. 5. The steady version of Eq. (18) for the drag coefficient is

$$F_x = 2\pi\int_0^1 [p](s)s\cos^2\alpha ds. \tag{27}$$

$$F_x \sim \mathcal{N}^{-1/2}\int_{-\infty}^{0}[P](S)SdS. \tag{28}$$

The axisymmetric problem has some important differences from the two-dimensional case studied in Refs. 4 and 5. In the two-dimensional case, a flexible fiber is clamped perpendicularly to the flow at its midpoint. The fiber's shape is described by its curvature, a one-dimensional function of the arc length. The cone, however, is described by a single parameter, its angle with the x axis. In both cases, the problem tends to a singular limit as $\mathcal{N}$ (or η^2 in Refs. 4 and 5) $\to\infty$. In the singular limit of the two-dimensional problem, the fiber is folded in half, leaving a divergent curvature at its midpoint. The flow is everywhere uniform and at the free stream speed except at the fiber midpoint, which is a stagnation point. The asymptotic behavior of the problem as $\mathcal{N}\to\infty$ is determined by the flow in a shrinking region near the fiber midpoint.

For the axisymmetric problem, as $\mathcal{N}\to\infty$, $\alpha\to-\pi/2$, i.e., the cone rolls up more tightly. The elastic energy divergence occurs everywhere along the cone surface, instead of being confined to a small region at the center as for the fiber. The flow meets the center of the fiber at a right angle, while the flow near the cone center is more similar to the flow past a wedge in two dimensions. In the limit that $\alpha\to-\pi/2$, the cone is more streamlined at the center than is the fiber. Consequently, there is a smaller pressure force at the center of the cone. Also, the region near the center of the cone contributes a proportionately smaller part of the total force on the cone because in cylindrical coordinates the area element of the cone increases with the arc length distance from the center, unlike for the fiber.

We have found good agreement with the experimental data of Ref. 7 in the scaling of both angle and drag with respect to $\mathcal{N}$. Our model's results differ from the models in Ref. 7 in the appearance of a self-similar form of the solution near the trailing edge wake of the cone, which appears to set the scaling of shape and drag. By contrast, the potential flow model in Ref. 7 assumed a potential flow in an infinite conical domain, with no vortex wake. In comparison with the models in Ref. 7, we have (somewhat surprisingly) found the same $\mathcal{N}^{-1/6}$ scaling of the angle's deviation from vertical, but a somewhat less rapid decrease of the drag coefficient, $\mathcal{N}^{-1/2}$ here versus $\mathcal{N}^{-2/3}$ in Ref. 7. Vogel found scalings of $\mathcal{N}^{-0.10}$ $-\mathcal{N}^{-0.59}$ for various broad leaves and clusters of leaves at flow speeds ranging from 10 to 20 miles/h in a wind tunnel.[2,3] In our two-dimensional model of the flexible fiber,[4,5] the profile area decreased as $\eta^{-1/3}\sim\mathcal{N}^{-1/6}$, which is also how profile area scales with $\mathcal{N}$ for the cone. The drag coefficient for the two-dimensional case scales as $\eta^{-2/3}$ $\sim\mathcal{N}^{-1/3}$, which is a slower decrease than the $\sim\mathcal{N}^{-1/2}$ behavior we have found for the cone.

[1] E. de Langre, "Effects of wind on plants," Annu. Rev. Fluid Mech. **40**, 141 (2008).
[2] S. Vogel, *Life in Moving Fluids*, 2nd ed. (Princeton University Press, Princeton, NJ, 1994).
[3] S. Vogel, "Drag and reconfiguration of broad leaves in high winds," J. Exp. Bot. **40**, 941 (1989).
[4] S. Alben, M. Shelley, and J. Zhang, "Drag reduction through self-similar bending of a flexible body," Nature (London) **420**, 479 (2002).
[5] S. Alben, M. Shelley, and J. Zhang, "How flexibility induces streamlining in a two-dimensional flow," Phys. Fluids **16**, 1694 (2004).
[6] L. Zhu, "Scaling laws for drag of a compliant body in an incompressible viscous flow," J. Fluid Mech. **607**, 387 (2008).
[7] L. Schouveiler and A. Boudaoud, "The rolling up of sheets in a steady flow," J. Fluid Mech. **563**, 71 (2006).
[8] G. K. Batchelor, *An Introduction to Fluid Dynamics* (Cambridge University Press, Cambridge, 1967).
[9] F. Gosselin, E. de Langre, and B. A. Machado-Almeida, "Drag reduction of flexible plates by reconfiguration," J. Fluid Mech. **650**, 319 (2010).
[10] M. Nitsche and R. Krasny, "A numerical study of vortex ring formation at the edge of a circular tube," J. Fluid Mech. **276**, 139 (1994).
[11] P. Saffman, *Vortex Dynamics* (Cambridge University Press, Cambridge, 1992).
[12] S. Alben, "Simulating the dynamics of flexible bodies and vortex sheets," J. Comput. Phys. **228**, 2587 (2009).
[13] M. Jones, "The separated flow of an inviscid fluid around a moving flat plate," J. Fluid Mech. **496**, 405 (2003).
[14] R. Krasny, "Desingularization of periodic vortex sheet roll-up," J. Comput. Phys. **65**, 292 (1986).
[15] R. Krasny and M. Nitsche, "The onset of chaos in vortex sheet flow," J. Fluid Mech. **454**, 47 (2002).
[16] B. Thwaites, *Incompressible Aerodynamics: An Account of the Theory and Observation of the Steady Flow of Incompressible Fluid Past Aerofoils, Wings, and Other Bodies* (Dover, New York, 1987).